Research Square

Preprints are preliminary reports that have not undergone peer review.
They should not be considered conclusive, used to inform clinical practice,
or referenced by the media as validated information.

# Ecologically safe microplastic removal from saline water via temperature and buoyancy separation

**Mehdi V. Bozorg**
Australian National University
**Juan Felipe Torres**
felipe.torres@anu.edu.au

Australian National University

**Article**

**Keywords:**

**Posted Date:** November 16th, 2026

**DOI:** https://doi.org/10.21203/rs.3.rs-11519635/v1

**License:** This work is licensed under a Creative Commons Attribution 4.0 International License.
Read Full License

**Additional Declarations:** No competing interests reported.

# Ecologically safe microplastic removal from saline water via temperature and buoyancy separation

Mehdi V. Bozorg[1] and Juan F. Torres[*1]

[1]ANU HEAT Lab, School of Engineering, The Australian National University, Canberra, Australia
[*]E-mail: felipe.torres@anu.edu.au

## Abstract

Although microplastics affect the atmosphere–ocean carbon cycle, the health of marine ecosystems, and pollute the food chain, existing microplastic removal methods cannot cope in the presence of microorganisms, particularly when there is an overlap in size. This is a technical challenge for the bio-friendly extraction of microplastics using conventional mechanical methods, such as a mesh. Here, we introduce a mesh-free, ecologically safe method that combines thermotactic and geotactic migration of biological species with controlled hydrodynamics to selectively separate microorganisms and microplastics of overlapping size. The microorganisms were one-day-old *Artemia* nauplii, an aquatic crustacean, and the microplastics were polyethylene spheres with a similar size range, approximately $307\,\mu\mathrm{m}$ to $450\,\mu\mathrm{m}$. By controlling the temperature differential in a rectangular channel flow up to $30\,\mathrm{K}$ and its flow rate up to $1208\,\mathrm{mL\,min^{-1}}$, a continuous process was achieved with microplastic removal efficiency and microorganism recovery rates as high as 90.4% and 70.7%, respectively. We report the trade-off between separation performance and the specific energy consumption, the latter being as low as $4.67\,\mathrm{kWh\,m^{-3}}$. Requiring no additional separation agents or functional materials, our method can provide a simple approach for sustainable, bio-friendly, in-situ microplastic remediation.

## Figures

**Fig. 1** Bio-friendly separation of microplastics from microorganisms: challenges, proposed solution and transport mechanisms 16
**Fig. 2** Thermal response of *Artemia* (brine shrimp) in a convectionless environment . . . . . 16
**Fig. 3** Gravimetric separation analysis of individual species in saline: *Artemia*, light (LP) and heavy (HP) microplastics . . 17
**Fig. 4** Computational fluid dynamics (CFD) modelling of MP transport in the rectangular channel . . . . . 18
**Fig. 5** Experimental and numerical visualisation of single constituents in saline . . . . . 19
**Fig. 6** Separation in a mixture of *Artemia*, light and heavy microplastics . . . . . 20

# 1 Introduction

Microplastics (MPs) — plastic debris from 1 µm to 5 mm in size — are polluting oceans and disrupting marine ecosystems at an unprecedented scale[1,2]. Microplastics may cause centuries-long ocean deoxygenation[3], i.e. North Pacific water-column oxygen loss[4]. Roughly 8 million tonnes of plastic waste enter the ocean annually[5], with MPs forming a substantial, dominant fraction of marine plastic particles[6]. This is both a climate and ecological problem: MPs induce phytoplankton toxicity[7] and reduced photosynthesis at high concentrations[8], undermining a group that supplies roughly half of Earth's oxygen[9] and, together with zooplankton grazing, drives the ocean's biological carbon pump[10,11]. Ingestion of MPs by zooplankton such as copepods and *Artemia* nauplii (brine shrimp) alters faecal pellet density[12], sinking rate[13,14], and structural integrity[14], impairing long-term carbon sequestration[14], while the same pathway transfers sorbed heavy metals[15], polycyclic aromatic hydrocarbons[16], and persistent organic pollutants[17–19] up the food chain — MPs have since been detected in human blood and across a wide range of tissues[20].

Conventional MP-removal methods fall into three categories: physical (filtration, flotation, sedimentation, adsorption), chemical (coagulation, flocculation, digestion, and density separation in concentrated NaCl or NaI brines), and biodegradation (bacteria-aided processes)[21]. MP capture efficiency has been improved by more recent approaches — acoustic focusing in microfluidic channels[22], electrokinetic separation using bipolar-electrode-induced electric-field gradients in a bifurcation channel[23], density- and size-resolved magnetic levitation[24], air-flotation-assisted hydrocyclones[25], laser photodegradation[26], focused sunlight[27], superhydrophobic sponges[28], hydrophobic bio-sorbents[29], and electrocoagulation[30,31]. However, all existing methods were developed and validated on MP-only suspensions, with none designed to discriminate MPs from co-suspended microorganisms (MOs) such as zooplankton. Critically, these methods rely on properties largely shared by MPs and MOs — such as size, density, surface charge, and hydrophobicity — making selective separation without harm inherently difficult. Mesh-based mechanical separation fails for the same reason: as Fig. 1a shows, roughly 55% of Atlantic MPs fall within 250 µm to 750 µm[32], overlapping the size range of young zooplankton[33]. Fig. 1b–c shows this size distribution overlaps directly for our proof-of-concept species — one-day-old *Artemia* nauplii and spherical polyethylene MPs (additional size metrics in Supplementary Fig. 1) — confirming that mesh separation cannot selectively and safely separate them, e.g. in Fig. 1d.

We hypothesise that the challenge of separating species of overlapping size distribution can be addressed by exploiting a property microorganisms possess but microplastics do not: thermotactic behaviour, which is an active, directed response to a temperature differential. This response is observed across diverse zooplankton taxa[34], including *Artemia*, which migrates toward cooler water under a temperature gradient (negative thermotaxis)[35]. Since prolonged exposure to 35 °C for 24 h cuts survival to about 25%[36], a mild stimulus of short exposure time can be applied without compromising the survival rate. Because the transport of MPs with particle size exceeding 5 µm is largely governed by flow field and buoyancy[37,38], i.e. thermophoresis can be neglected for MPs larger than 5 µm, the thermotaxis of microorganisms can decouple MP and microorganism transport. A methodology informed by bio-transport and fluid dynamics can enable a chemical-free, non-invasive separation strategy independent of size or density.

This research proposes and demonstrates a bio-friendly MP removal method based on a hydro-thermal process — no phase-change, chemicals, or functional materials — underpinned by zooplankton thermal preference and the hydrodynamic response of MPs in a non-isothermal flow through a simple rectangular duct. We first investigated the thermotactic response of *Artemia* in a convectionless cell under varying top-to-bottom temperature differences, then examined individual constituents — *Artemia*, light (LP) and heavy (HP)

microplastics — in saline duct flow under isothermal and non-isothermal conditions across flow rates. We combined gravimetric and image-processing experiments with computational fluid dynamics (CFD) modelling of MPs. Finally, we tested separation of MPs from *Artemia* in a multicomponent suspension at a 30 K temperature differential, i.e. the temperature difference between the upper and lower channel walls, achieving high MP removal alongside high *Artemia* recovery. The specific energy consumption of the process was computed and found comparable with widely used water treatment technologies and compatible with solar-powered, scalable in-situ remediation, without requiring additional separation materials, supporting its potential as a sustainable, MP remediation technology.

# 2 Results

We propose and assess a simple bio-friendly separation method based on the thermotactic migration of *Artemia* and controlled hydrodynamics of MPs. The process occurs in a rectangular duct flow with the upper wall actively heated and the lower wall cooled, as shown conceptually in the schematic of Fig. 1e. The forces acting on *Artemia* and MPs close to and far from the walls are shown in Fig. 1f. Positive thermotaxis refers to the swimming of *Artemia* towards the upper hot wall. In contrast, negative thermotaxis, positive geotaxis, and buoyancy-driven precipitation promote their downward migration toward the lower cold wall. MP transport, by contrast, is governed primarily by the balance of buoyancy, drag, and particle–wall interaction forces (further hydrodynamic details in Supplementary Methods 1).

## 2.1 Thermal response of *Artemia* in stagnant saline

Before exploring a channel flow that enables a continuous separation process, the thermal response of one-day-old *Artemia* in a convectionless saline solution was investigated using the experimental setup schematically illustrated in Fig. 2a. Details of the experimental procedure and result post-processing are provided in the Methods section. Figure 2b shows the distribution of *Artemia* on a vertical plane under isothermal condition (left) and temperature gradient stressors — with temperature differential up to $\Delta T_{\mathrm{wall}} = 30\,\mathrm{K}$ keeping the lower wall temperature at $20\,^{\circ}\mathrm{C}$. Compared with the isothermal condition, applying a thermally stabilising temperature differential (by heating and cooling the upper and lower walls, respectively) induced negative thermotaxis in *Artemia*, i.e. migration towards the colder region. This increased the number density of *Artemia* in the bottom of the cell. Thermotactic migration of *Artemia* increased with $\Delta T_{\mathrm{wall}}$. Noting the temperature profiles of the upper and lower walls in Fig. 2c, the upper wall temperature reached the set temperature after approximately $4\,\mathrm{min}$, whereas the bottom-wall temperature gradually increased due to insufficient cooling by the bottom Peltier module, leading to a decrease in $\Delta T_{\mathrm{wall}}$. Consequently, as shown in Fig. 2b, the shrimp population in the upper half of the cell at $t = 8\,\mathrm{min}$ was higher than that at $4\,\mathrm{min}$ under the non-isothermal conditions.

To quantify the separation behaviour of *Artemia*, the separation ratio or the microorganism, $SR_{\mathrm{O}}$, was defined as follows

$$SR_{\mathrm{O}} = \frac{C_{\mathrm{btm}} - C_{\mathrm{top}}}{C_{\mathrm{btm}} + C_{\mathrm{top}}}, \tag{1}$$

where $C_{\mathrm{btm}}$ and $C_{\mathrm{top}}$ are the concentration of *Artemia* in the bottom and top halves of the convectionless cell, respectively. As the volume of the top and bottom halves is identical, and assuming that *Artemia* nauplii weigh the same, Eq. (1) is computed from image processing by counting the number of *Artemia* nauplii in each half (see Methods). $SR_{\mathrm{O}} = 0$, 50, and 100% corresponds to 50%

(homogeneous distribution), 75%, and 100% (complete separation), respectively, of *Artemia* nauplii accumulated in the bottom half of the cell. Figure 2d shows the measured temporal variability in $SR_{\mathrm{O}}$ for increasing temperature differential; $SR_{\mathrm{O}}$ at $\Delta T_{\mathrm{wall}} = 25\,\mathrm{K}$ and $30\,\mathrm{K}$ are considerably higher than that at $20\,\mathrm{K}$, indicating that *Artemia* preferred the bottom half of the cell adjacent to the lower cold wall at $20\,^{\circ}\mathrm{C}$. Importantly, this preference was more pronounced as the temperature gradient stressor was increased, which is attributed to the negative thermotaxis of *Artemia* (migration towards the colder region) triggered by the heated upper wall. In contrast, under isothermal conditions, $SR_{\mathrm{O}}$ remained below 5%, indicating an approximately equal distribution of *Artemia* in the cell.

## 2.2 Gravimetric separation analysis of individual species in a channel flow: *Artemia* and microplastics

Figure 3a shows the experimental setup to test the continuous and selective separation of *Artemia* and MPs using a duct flow with a controlled temperature differential $\Delta T_{\mathrm{wall}}$. First, we characterise the transport behaviour of individual species as the building block of the proposed bio-friendly MP removal method.

The top and bottom stream samples were collected and analysed following the procedure depicted in Fig. 3b (details in Methods section). Figure 3c presented the measured *SR* over a wide range of flow conditions for each species passed individually. Under an isothermal flow, *Artemia* exhibited positive geotaxis, i.e. migration towards the bottom wall in the direction of gravity, and *SR* remained approximately constant up to $\bar{u} = 23.1\,\mathrm{mm\,s^{-1}}$. Supplementary Video 1a shows how *Artemia* nauplii tend to avoid the high-velocity central region and the upper wall, accumulating in the bottom half of the channel. In contrast, when the lower wall was heated, the expected upward thermotactic migration of *Artemia* (towards the cold wall) was suppressed by buoyancy-induced convection eddies that arise by the destabilising thermal stimuli[39] because their swimming velocity was insufficient to overcome the buoyancy-induced hydrodynamic eddies. Consequently, a small *SR* was obtained (purple hollow downward-pointing triangles). In contrast, heating the upper wall thermally stratified the flow and facilitated the downward migration of *Artemia* nauplii, as their gravitational settling (positive geotaxis) and swimming towards the cold region (negative thermotaxis) were aiding factors. This configuration enabled *Artemia* to reach the colder bottom region even under a relatively strong flow (orange hollow up-pointing triangles). Yet the highest separation ratio in this case was 76%, obtained at the lowest tested flow speed of $\bar{u} = 2.6\,\mathrm{mm\,s^{-1}}$, which is comparable to the swimming velocity of *Artemia* reported in Ref. [37].

For MPs, the absolute value of *SR* was significantly high due to the positive and negative buoyancy-driven transport (circle and diamond markers in Fig. 3c). However, to achieve an efficient separation, the amount of MP extraction had to be sufficiently high. The extracted masses of LP and HP for two flow rates are shown in Fig. 3d and e for the top and bottom flow streams, respectively. CFD modelling results show a good agreement with the experimental data (Methods section presents the details on the high-fidelity CFD modelling). For LP, the cumulative mass under $\Delta T_{\mathrm{wall}} = 30\,\mathrm{K}$ was slightly higher than the isothermal case (Fig. 3d). In contrast, a differential of $30\,\mathrm{K}$ reduced HP extraction relative to the isothermal case (Fig. 3e).

Figure 4 shows the more detailed results of the CFD modelling, which was conducted to understand the competing factors in the MP transport phenomenon along the rectangular channel. The analysis was focused on analysing three competing mechanisms affecting MP transport: buoyancy, viscosity, and jet development from channel inlet. We found that viscous effects dominate the deposition length and creeping speed, which is the speed at which MP particle travel adjacent to the channel post-deposition. Figure 4, panel (I), confirms that buoyancy determine whether the MP particles sink or float (HP and LP, respectively), with the deposition length shortened by the

introduction of the $\Delta T_{\text{wall}}$ regardless of the MP density. This is because the viscosity decreased drastically in the heated channel (Supplementary Fig. 2a), which affected the velocity of the particles. As shown in Fig. 4 (panels I and II), the average streamwise particle velocity remained essentially the same under isothermal and heated conditions because the syringe pump prescribed the same volumetric flow rate in both cases. In contrast, the terminal velocity in the vertical direction increased due to reduced viscosity (Supplementary Fig. 3), which was the main cause of a shorter deposition length. Post-deposition on the vicinity of the walls, the MP creeping speed was determined by the local viscosity value. The creeping speed for LP particles was higher in the heated channel compared to the isothermal case, as shown in the inset of Fig. 4a(I), due to a lower viscosity adjacent to the upper hot wall, which contribute to the higher LP mass extraction observed experimentally (Fig. 3d). In contrast, the creeping speed of HP decreased in the non-isothermal case because the temperature adjacent to the lower cold wall was slightly lower than the isothermal case (Supplementary Fig. 2c), increasing viscosity and hence the decreasing the local velocity, thereby decreasing LP extraction compared with the isothermal conditions (Fig. 3e).

The viscosity also affected the jet developing length and flow behaviour, which played a role in MP dynamics. Figure 4, panels (III) and (IV), shows that the jet developing length expands in the heated channel compared to the isothermal case. Although this could result in an increased deposition length, albeit with the presence of stronger recirculation zones, viscous effects associated with terminal velocities dominated. Comparison with simulations in which the inlet jet was artificially removed (Supplementary Tables 4–5) confirms that the jet contributed to the increased deposition length of both LPs and HPs, i.e. 32% longer deposition length for HPs at $\bar{u} = 95.3\,\text{mm}\,\text{s}^{-1}$ (compare Fig. 4b(I) with Supplementary Table 5).

## 2.3 Spatial distribution analysis of individual constituents using image processing and CFD simulations

Experimental streamwise transport of *Artemia*, LPs, and HPs in single-constituent saline suspensions was visualised using the laser setup shown schematically in Fig. 5a (details of the experimental setup are found in the Methods section and Supplementary Fig. 4a). The spatial distribution of MP obtained in the experiments is compared with the CFD data. Figure 5b(I) shows *Artemia*'s *SR* as a function of time at different locations for $u = 2.6\,\text{mm}\,\text{s}^{-1}$ and $\Delta T = 30\,\text{K}$. At $135\,\text{mm}$ from the inlet, the value of *SR* is low and fluctuates substantially, which is attributed to strong mixing due to vortices near the inlet (see also Supplementary Fig. 4b(I)–(III) and Supplementary Video 2a). From Fig. 5b, at distances greater than $225\,\text{mm}$ from the inlet, *Artemia* effectively used geotaxis and active swimming to migrate thermotactically toward the colder bottom region, resulting in an image-processing-based *SR* of about $69.7\% \pm 7.2\%$, comparable to the weighted-based *SR* of $75.8\% \pm 3.0\%$ obtained using the procedure shown in Fig. 3b(II). Raw and processed videos of *Artemia* transport at $x_5$ are provided in Supplementary Video 2b.

Figure 5c shows snapshots of the LP distribution on the mid-vertical plane along the channel, visualised in the experiments under isothermal conditions of $22.7\,^{\circ}\text{C}$ and $\bar{u} = 35.3\,\text{mm}\,\text{s}^{-1}$, while Fig. 5d shows the corresponding CFD data. Likewise, the experimental and CFD transport of HPs at $22.9\,^{\circ}\text{C}$ and $\bar{u} = 82.9\,\text{mm}\,\text{s}^{-1}$ is shown in Figs. 5e and f, respectively. Following the initial settling phase, the particles travelled in contact with the upper wall for LPs (Fig. 5c, d(I)) and the lower wall for HPs (Fig. 5e, f(I)). In the experiments, a small fraction remained slightly away from the wall. In contrast, all particles in the CFD simulations travelled in contact with the respective walls after settling (Figs. 5d(I) and f(I) for LPs and HPs, respectively). This indicates a variability in MP density used in the experiments. Supplementary Video 2c, d show the experimental visualisation for LP and HP around $x_3$ and $x_4$, respectively. As shown

in Figs. 5d(I) and f(I), backward particle movement was observed near the inlet, induced by multiple clockwise and counter-clockwise recirculation zones generated by the inlet jet in the near-inlet region ($x \lesssim 150\,\mathrm{mm}$). These recirculation zones are evident from the $y$-direction velocity contours of the bulk fluid shown in Figs. 5d(II) and f(II). The variation of *SR* along the channel length obtained from image processing and CFD is presented in Figs. 5g and h for LPs and HPs, respectively, together with the *SR* values obtained gravimetrically from filtered samples at the outlets ($x = 500\,\mathrm{mm}$). As shown in Figs. 5g and h, the effect of the inlet-induced recirculation zones is reflected in fluctuations in *SR* within the near-inlet region ($x \lesssim 150\,\mathrm{mm}$). These results indicate that, for a channel height of $9\,\mathrm{mm}$ and velocity below $\bar{u} = 40\,\mathrm{mm\,s^{-1}}$, the rectangular channel should be longer than $250\,\mathrm{mm}$ to enable a separation.

## 2.4 Separation of microplastics from zooplanktons in non-isothermal rectangular flow

We propose a multi-stage process to achieve a bio-friendly separation of LPs and HPs from saline containing *Artemia*, based on their hydrodynamic and thermo-geo-tactic transport control. The concept design is based on the data of Fig. 3c, whereby *Artemia*, LPs, and HPs in a single-constituent saline suspension separated at different rates over different ranges of average velocities. Each stage is characterised by an average flow velocity: low $\bar{u}_1$ is comparable to that of swimming *Artemia*, moderate $\bar{u}_2$ still allows *Artemia* response, and strong $\bar{u}_3$ flushes any remaining MPs in the channel. The feed composition and flow conditions for the three-stage and two-stage processes are shown in Fig. 6a. The collection during Phase A and Phase B and subsequent gravimetric measurement of *Artemia* and microplastics are depicted in Fig. 6b, together with the separation metrics. In the proposed multi-stage separation processes, Phase A was designed to remove *Artemia*, whereas Phase B was aimed at MP removal. Phase A in the two-stage process comprised mixture loading ($L_{\mathrm{O+P}}^{\mathrm{Q2}}$) at an average velocity of $\bar{u}_2 = 16.5\,\mathrm{mm\,s^{-1}}$ or $23.1\,\mathrm{mm\,s^{-1}}$. Phase A of the three-stage process comprised mixture loading ($L_{\mathrm{O+P}}^{\mathrm{Q1}}$) at an average velocity of ($\bar{u}_1 = 2.6\,\mathrm{mm\,s^{-1}}$), followed by Stage 2, which was used to load the residual MP–microorganism mixture from the syringe after Stage 1 and flush the microorganisms remaining in the channel from Stage 1 ($(L_{\mathrm{O+P}}F_{\mathrm{O}})^{\mathrm{Q2}}$) at $\bar{u}_2 = 16.5\,\mathrm{mm\,s^{-1}}$ or $23.1\,\mathrm{mm\,s^{-1}}$, extracting the remaining *Artemia*. Phase B involved the MP flushing stage ($F_{\mathrm{P}}^{\mathrm{Q3}}$) in both two- and three-stage processes. Based on the correlations of the separation parameters presented in Method section, $SR_{\mathrm{O,A}}$ and $SR_{\mathrm{P,A}}$ represent the *Artemia* and MP separation ratios in Phase A, respectively; $\eta_{\mathrm{O}}$ and $\eta_{\mathrm{P}}$ denote the separation efficiencies of *Artemia* and MPs, respectively. Higher $\eta_{\mathrm{P}}$ reduces the amount of MP contamination in the recovered *Artemia*, the latter quantified by $\eta_{\mathrm{O}}$. The overall separation efficiency $\eta$ considers both contributions, MP removal and *Artemia* survival, i.e. $\eta = \eta_{\mathrm{O}} \times \eta_{\mathrm{P}}$

The separation parameters for the two- and three-stage processes at moderate $\bar{u}_2$ of $16.5\,\mathrm{mm\,s^{-1}}$ and $23.1\,\mathrm{mm\,s^{-1}}$ are shown in Fig. 6c. In contrast to the two-stage process, the three-stage process exhibited a higher $SR_{\mathrm{O,A}}$ attributed to the low-velocity loading stage, which enables more efficient thermotactic migration of *Artemia*. Recall that *Artemia* has positive geotaxis and negative thermotaxis (both migrations towards the bottom when heating the upper wall), as observed in the single-constituent experiments of Figs. 2, 3, and 5. In addition, the higher $\bar{u}_2$ yielded a lower $SR_{\mathrm{O,A}}$, likely due to mixing effects caused by the increased flow either because of a reduction of thermotactic migration, increased developing length, vortex mixing, or a combination of these factors. $SR_{\mathrm{P,A}}$ was significantly higher for the three-stage process because of the greater LP extraction from the top outlet achieved at the end of Phase A (compare Supplementary Tables 1—2). Due to the greater density difference between saline and HPs, HPs did not reach the outlet by the end of Phase A. Regarding the separation efficiencies of the multi-stage processes (considering both phases), Fig. 6c shows the three-stage separation with $\bar{u}_2 = 23.1\,\mathrm{mm\,s^{-1}}$ resulted in the highest overall separation efficiency of $\eta = 63.8\% \pm 10.1\%$, with the highest $\eta_{\mathrm{O}}$ of

$70.7\% \pm 11.2\%$ being 26.8% higher than that of the same process at $\bar{u}_2 = 16.5\,\mathrm{mm\,s^{-1}}$ due to the lower amount of residual *Artemia* remaining in the channel at the end of Phase B (Supplementary Table 2); while MP removal efficiencies are approximately the same.

The scalability of a process is largely dependent on its energy consumption. Figure 6d shows that, despite achieving higher separation efficiencies, the three-stage processes had a significantly higher specific energy consumption (SEC) than the two-stage processes, i.e. 5.3 and 6.3 times higher for $\bar{u}_2 = 16.5\,\mathrm{mm\,s^{-1}}$ and $23.1\,\mathrm{mm\,s^{-1}}$, respectively. This is because the lower loading velocities required heating and cooling of the upper and bottom walls for longer periods. The SEC for the two-stage process was as low as $4.67\,\mathrm{kWh\,m^{-3}}$, which is comparable with large-scale desalination via reverse osmosis. This suggests that the process can be scaled in a similar fashion provided there is an economic incentive to implement.

The critical design parameters affecting separation efficiency are: (I) the channel length, which must considerably exceed both the hydrodynamic entrance length (Supplementary Table 3) and the MP deposition lengths (Supplementary Tables 4–5 — excluding the MP flushing stage), and (II) the channel height, which must provide an appropriate distance for thermotactic migration of *Artemia* to occur (Fig. 2b). Consequently, channel width is the parameter best suited for scaling up. Alternatively, a separation unit with multiple parallel channels multiplies the MP remediation capacity. For example, a two-stage process with 20 parallel channels achieves 5.1 times the daily MP remediation capacity of the three-stage process, with 19.7% lower daily energy consumption (Supplementary Fig. 5). The energy demand for 20 parallel channels can be met by a small-scale domestic PV system of approximately $4.3\,\mathrm{kWp}$ powering a chiller and water heater, and could be reduced further by coupling the PV system with solar thermal or a heat pump. The modular, continuous operation without requiring chemical or material additives supports the potential for large-scale, sustainable in-situ treatment of MP-contaminated water with reduced harm to biological species.

# 3 Discussion

We propose and demonstrate a bio-friendly method to separate microplastics (polyethylene MPs) from small crustacean zooplankton (*Artemia*) by applying a moderate temperature differential of $\Delta T_{\mathrm{wall}} \leq 30\,\mathrm{K}$ across a saline with a wide range of flow through a rectangular channel or duct. The separation channel is comprised of a simple rectangular duct whose upper and lower walls can be thermotactically controlled. Unlike existing removal technologies, our approach demonstrates its bio-compatibility. By tuning feed hydrodynamics and *Artemia* thermotactic migration, combined with particle–wall interactions, enables effective separation from MPs.

## 3.1 Selection of operating temperatures

Our experimental trials show that a temperature of $50\,^{\circ}\mathrm{C}$ is safe for *Artemia*, with the upper hot wall set to $50\,^{\circ}\mathrm{C}$ and lower cold wall to $20\,^{\circ}\mathrm{C}$. This is consistent with the literature where heat-shock trials are reported from $22\,^{\circ}\mathrm{C}$ to $50\,^{\circ}\mathrm{C}$ with complete embryo survival[40], consistent with $50\,^{\circ}\mathrm{C}$ triggering a strong protective heat-shock protein (HSP) response — nuclear translocation of p26 — without mortality[41]. In the convectionless cell (Fig. 2a), we also tested moderate temperature differentials ($10\,\mathrm{K}$ and $15\,\mathrm{K}$), a lower wall temperature of $25\,^{\circ}\mathrm{C}$, and sparse and dense populations. In all cases, *Artemia* still showed thermotactic migration towards the lower cold wall (Supplementary Fig. 6), although slow equilibration in some trials (approximately $50\,\mathrm{min}$) may have added oxygen-deficiency effects. These trials show that MP separation is feasible under weaker temperature differentials. Although the separation efficiency can

be reduced due to a weaker thermotactic migration under a smaller $\Delta T_{\mathrm{wall}}$, the latter reduces the risk of thermal shock and the specific energy consumption (SEC) compared to a large $\Delta T_{\mathrm{wall}}$. Our single-constituent experiments of *Artemia* transport in the rectangular channel at $\bar{u} = 2.6\,\mathrm{mm\,s^{-1}}$ under $\Delta T_{\mathrm{wall}} = 10\,\mathrm{K}$ (lower and upper wall temperatures of $30\,^{\circ}\mathrm{C}$ and $40\,^{\circ}\mathrm{C}$, respectively) and $\Delta T = 20\,\mathrm{K}$ (lower and upper walls at $25\,^{\circ}\mathrm{C}$ and $45\,^{\circ}\mathrm{C}$, respectively) are shown in Supplementary Video 3. These experiments yielded *SR* values of 40.3% and 47.4%, considerably lower than the $> 72\%$ observed for $\Delta T_{\mathrm{wall}} = 30\,\mathrm{K}$ (Fig. 3c).

## 3.2 Applicability beyond *Artemia*

We used *Artemia* as the model microorganism for its ease of hatching and cyst availability in Australia; whether this approach extends to other species remains an open question. Thermotactic behaviour has been demonstrated across nine aquatic species over a temperature differential between $20.5\,^{\circ}\mathrm{C}$ to $39\,^{\circ}\mathrm{C}$, with most preferring the cooler temperature of about $24\,^{\circ}\mathrm{C}$ while avoiding that above $27\,^{\circ}\mathrm{C}$ (Ref. [35]). In addition, *Callinectes sapidus* larvae exposed to a vertical differential between $15.0\,^{\circ}\mathrm{C}$ and $35.0\,^{\circ}\mathrm{C}$ occupied $> 90\%$ of the lower cold region[42]. This reported thermal preference or thermotaxis in a broad range of species suggests the proposed bio-friendly MP removal strategy extends beyond *Artemia* to other aquatic microorganisms with similar thermal preferences. However, the maximum safe temperature (e.g. $50\,^{\circ}\mathrm{C}$ for *Artemia*) should be examined in future work with microorganisms. For example, temperatures above $33\,^{\circ}\mathrm{C}$ were reported fatal to larvae of starfish bipinnaria (phylum Echinodermata)[43], though that study used a less-favourable horizontal differential and a narrower $26\,^{\circ}\mathrm{C}$–$36\,^{\circ}\mathrm{C}$ range. Importantly, a vertical temperature differential between $20\,^{\circ}\mathrm{C}$ and $50\,^{\circ}\mathrm{C}$ does not necessarily expose microorganisms to $50\,^{\circ}\mathrm{C}$: the fluid bulk, even a short distance from the upper wall, is significantly cooler than $50\,^{\circ}\mathrm{C}$ (Supplementary Fig. 2c(II)), and negative thermotaxis lets microorganisms actively migrate away from these warmer regions, further limiting the time they are exposed to the maximum temperature.

## 3.3 Applicability to microplastics with different density ranges

The selected MP densities of $995\,\mathrm{kg\,m^{-3}} \pm 10\,\mathrm{kg\,m^{-3}}$ for light and $1090\,\mathrm{kg\,m^{-3}} \pm 5\,\mathrm{kg\,m^{-3}}$ for heavy MPs span a representative portion of the density range reported for oceanic MPs[44–46]. Oceanic MPs cover a broad density range[46], from low-density polymers such as polypropylene ($895\,\mathrm{kg\,m^{-3}}$ to $920\,\mathrm{kg\,m^{-3}}$), polyethylene ($917\,\mathrm{kg\,m^{-3}}$ to $965\,\mathrm{kg\,m^{-3}}$) and PEVA ($930\,\mathrm{kg\,m^{-3}}$ to $960\,\mathrm{kg\,m^{-3}}$) to denser polymers including PS ($1040\,\mathrm{kg\,m^{-3}}$ to $1060\,\mathrm{kg\,m^{-3}}$), PMMA ($1180\,\mathrm{kg\,m^{-3}}$), polyurethane ($1200\,\mathrm{kg\,m^{-3}}$), PVC ($1380\,\mathrm{kg\,m^{-3}}$ to $1400\,\mathrm{kg\,m^{-3}}$) and PET ($1300\,\mathrm{kg\,m^{-3}}$ to $1400\,\mathrm{kg\,m^{-3}}$)[44,45]. Accordingly, $995\,\mathrm{kg\,m^{-3}}$ represents a low-density, buoyant MP class spanning the upper end of commonly reported polyolefin densities, whereas $1090\,\mathrm{kg\,m^{-3}}$ represents a higher-density MP class close to the lower range of oceanic MPs and above the density of seawater (ca. $1025\,\mathrm{kg\,m^{-3}}$). That is, the light and heavy MPs used in this study had a density close to that of seawater, with $\Delta\rho$ approximately $30\,\mathrm{kg\,m^{-3}}$ for the light and $70\,\mathrm{kg\,m^{-3}}$ for heavy MPs. When the proposed method is applied to MPs with densities that differ significantly from that of seawater, the development length is expected to decrease as a result of stronger buoyancy-driven ascent or settling. The environmental relevance of the light-MP case is further supported by observations that buoyant MPs can occur throughout the water column, from the ocean surface to the deep sea through transport by marine snow (aggregates of organic matter, MO and particulate material including MP that continuously sinks) and repeated aggregation–disaggregation cycles[47]. Therefore, low-density MPs cannot be assumed to remain exclusively near the surface, and the selected $995\,\mathrm{kg\,m^{-3}}$ density is relevant to MPs that may be encountered at different ocean depths.

### 3.4 Pathways towards sustainable and scalable microplastic removal

The operating temperatures required for separation, between $20\,^{\circ}\mathrm{C}$ and $50\,^{\circ}\mathrm{C}$, as well as the heat fluxes normal to the flow, $2.01\,\mathrm{kW\,m^{-2}}$ and $2.22\,\mathrm{kW\,m^{-2}}$, for cooling and heating respectively, are moderate and can be easily maintained using renewable energy. Two renewable-energy approaches could provide the required thermal management: a photovoltaic-thermal (PVT) system could supply solar heat directly to the $50\,^{\circ}\mathrm{C}$ wall while its photovoltaic output powers a compact refrigeration unit for the $20\,^{\circ}\mathrm{C}$ wall, i.e. a $100\,\mathrm{W}$ PVT system coupled with active chilled-water cooling was experimentally investigated[48]. Alternatively, photovoltaic electricity could drive a heat pump that simultaneously extracts heat from the cold side and transfers it to the hot side, reducing the electrical energy required for separate heating and cooling[49]. Both approaches could therefore enable renewable-energy-powered operation while maintaining the required temperature differential.

The peak thermal requirement of the three-stage process, based on our CFD results, was $30.46\,\mathrm{kW\,h\,m^{-3}}$, corresponding to approximately $29\,\mathrm{W}$ for heating and $27\,\mathrm{W}$ for cooling in our proof-of-concept experimental setup. These requirements indicate that both proposed renewable-energy configurations could be readily scaled to support larger-scale operation of the separation process, i.e. a PVT system demonstrated simultaneous production of hot water at $76.61\,^{\circ}\mathrm{C}$ and chilled water at $15\,^{\circ}\mathrm{C}$, with $3777.5\,\mathrm{W}$ of thermal power extracted by the hot water and $931.11\,\mathrm{W}$ of cooling power, respectively[50]. In addition, a domestic-scale PVT system was tested, providing approximately $600\,\mathrm{W}$ of thermal power and $200\,\mathrm{W}$ of electrical power for approximately $8\,\mathrm{h}$[51]. Requiring no chemical separation agents, applied electrical or magnetic fields, or size-selective membranes, and driven by thermal loads well within reach of local solar energy resources, our proposed ecologically safe MP removal approach is, in principle, compatible with direct in-situ deployment and a wide range of MPs and MOs. This offers a pathway toward sustainable, ecosystem-safe large-scale remediation of MP pollution.

## 4 Methods

### Statistics and reproducibility

For the channel-flow experiments, each condition was evaluated gravimetrically using $n = 5$–$8$ independent runs. Each run used a freshly prepared *Artemia*–MP suspension and was treated as an independent experimental replicate. Reported separation ratios and efficiencies for these experiments are the mean $\pm$ one standard deviation across independent runs. For the convectionless-cell experiments (Fig. 2), each temperature-differential condition was evaluated in a single experimental run; 12–15 images acquired during that run were analysed to compute the separation ratio at each time point. These images are repeated measurements within one run and are not independent experimental replicates. The measurement reported in Fig. 2d are intended as a mechanistic demonstration rather than a quantitative basis for the performance claims of this work, which rest on the channel-flow data. The consistent, monotonic response of the separation ratio to $\Delta T_{\mathrm{wall}}$ across independently prepared cells supports the reproducibility of the effect, while the reported dispersion in Fig. 2d reflects within-run measurement variability only.

Experimental conditions were tested in a fixed sequence dictated by wall thermal-equilibration time (Fig. 2b–d) and by the need to complete testing within same-day testing window during which freshly hatched, age-matched *Artemia* nauplii were used. Separation ratios and masses were obtained from automated image-processing algorithms and analytical-balance measurements (not subjective

visual assessment). The number of independent runs in the channel-flow experiments was selected based on preliminary experiments and the reproducibility of the separation measurements.

## Hatching of *Artemia*

*Artemia*, widely known as brine shrimp, is hatched from cysts (AQUABUY) under controlled temperature conditions. $5\,\mathrm{g}$ of cysts were placed in a conical container filled with $1\,\mathrm{L}$ of aqueous NaCl solution. The NaCl solution was gravimetrically prepared with NaCl (EMSURE®, argentometric assay showing purity of $\geq 99.5\%$) and deionised water at room temperature at a concentration of about $3.4\,\mathrm{wt}\%$. A $100\,\mathrm{W}$ aquarium heater was used to maintain the saline temperature at $25\,^{\circ}\mathrm{C} \pm 1\,^{\circ}\mathrm{C}$ during hatching, with continuous aeration from the bottom. The heater was removed after $24\,\mathrm{h}$. After approximately $48\,\mathrm{h} \pm 2\,\mathrm{h}$ from the start of hatching, aeration was stopped. After $5\,\mathrm{min}$, most of the unhatched cysts and empty cyst shells floated to the surface and were removed using a syringe. Aeration was then resumed, and the experiments were conducted within one day using the remaining saline suspension containing *Artemia* nauplii. Based on an observed hatching time of about $24\,\mathrm{h}$, the *Artemia* nauplii were approximately one-day old ($28\,\mathrm{h} \pm 5\,\mathrm{h}$) at the time of the experiments.

## Convectionless cell setup

The experimental setup (Fig. 2a) uses two $18.2\,\mathrm{W}$ Peltier modules (European Thermodynamics APC-127-10-24-S-F4) mounted on two copper plates, which served as the upper and lower walls of the cell, to maintain the walls at the prescribed temperatures[52]. Two switching-mode power supplies ($0\,\mathrm{V}$ to $18\,\mathrm{V}$, $0\,\mathrm{A}$ to $20\,\mathrm{A}$) independently powered the Peltier modules. Two H-bridge circuits were placed between the power supplies and the Peltier modules to reverse the direction of the current through the modules. The H-bridge circuits were connected to a microprocessor (Arduino Mega 2560 Rev 3) to control the operation of the Peltier modules. To provide the controller with the temperatures at the centre of the top and bottom copper blocks, two K-type thermocouples were connected to two thermocouple amplifiers (Adafruit Universal MAX31856), which were then connected to the microprocessor. The test cell was a $10\,\mathrm{mm}$-cubic acrylic enclosure. Two fins were directly connected to the Peltier modules and served as heat sinks. The bottom fin was cooled using two axial fans.

The *Artemia* distribution image (e.g. Fig. 2b) were acquired using a CMOS camera (Basler ace2, Color USB3 Pro) equipped with a magnifying lens (AVENIR TV, $12.5\,\mathrm{mm}$ to $75\,\mathrm{mm}$, F1.8). To quantify the separation ratio within the cell, a MATLAB image-processing code was developed in-house. The *SR* value at each time point was determined by analysing 10–15 images. For the results presented in Supplementary Fig. 6, a CMOS camera (Allied Vision Manta GigE) was used. Although a lower target temperature difference was applied in these experiments, using a single power supply to control both Peltier modules resulted in a longer time to reach the set temperatures.

## Preparation of the microplastic suspension

Red fluorescent spherical polyethylene particles (Cospheric) were used as light and heavy MPs. For both types, the supplier reported that more than 90% of the particles had diameters in the range of $355\,\mu\mathrm{m}$ to $425\,\mu\mathrm{m}$, with a nominal mean diameter of $390\,\mu\mathrm{m}$. The particle-size distributions were independently quantified from microscopic images (results in Fig. 1c(II)–(III)). The light MPs had a

supplier-reported density range of $985\,\mathrm{kg\,m^{-3}}$ to $1005\,\mathrm{kg\,m^{-3}}$. Following the separation experiments with light MP, particles collected using a mesh ($100\,\mu\mathrm{m}$) from the bottom outlet were dried and subsequently dispersed in a biosurfactant–DI water suspension. Almost all particles sank in the suspension, indicating that their densities exceeded the density of the surrounding fluid at room temperature ($995\,\mathrm{kg\,m^{-3}}$). This observation suggests that the tested light-MP population may include particles with densities above the upper limit of the nominal density range reported by the supplier, although the supplier did not specify the measurement uncertainty or accuracy. The heavy MPs had a nominal density of $1090\,\mathrm{kg\,m^{-3}}\ \pm 5\,\mathrm{kg\,m^{-3}}$.

To facilitate the suspension of MPs in saline, their hydrophilicity was improved by adding the biosurfactant cocamidopropyl betaine (CAPB) at a concentration of $200\,\mathrm{mg\,L^{-1}}$. This mimics the increased hydrophilicity of naturally biofouled ocean MPs, absent in the pristine, as-received particles used here; CAPB is a feed-preparation step and is not part of the separation mechanism itself. LP and HP were each used at a concentration of $160\,\mathrm{mg\,L^{-1}}$. The masses of the MPs and biosurfactant were measured using an analytical balance (Shimadzu ATX224) with a readability of $0.1\,\mathrm{mg}$ and a repeatability (standard deviation) of $0.1\,\mathrm{mg}$. To better understand the effect of CAPB concentration on the hydrophilicity of polyethylene MPs, contact angle tests for saline on a solid polyethylene surface were conducted (sessile drop test, Supplementary Fig. 7a). In addition, the survival of *Artemia* nauplii in saline containing four different biosurfactants was conducted, then down selecting CAPB as the biosurfactant of choice in this study (Supplementary Fig. 7b).

## Feed flow rate control

The mixture of $3.4\,\mathrm{wt}\%$ aqueous NaCl, MPs and/or *Artemia* was fed into the rectangular channel using a syringe pump designed in-house (labelled in Fig. 3a). The syringe pump was equipped with a linear stage actuator (RATTMMOTOR, EBX1605) of $500\,\mathrm{mm}$ in travel range and a stepper motor (NEMA 23) rated at $3\,\mathrm{A}$ and $1.2\,\mathrm{N\,m}$ torque. The flow rate was controlled using a stepper motor and driver, which regulated the linear displacement of the syringe plunger. A magnetic rod was placed inside the syringe and with the magnetic stirrer underneath it maintained a uniform suspension of the mixture. The syringe had a capacity of $1.5\,\mathrm{L}$.

## Controlling the temperature of the rectangular flow

The experimental setup consisted of three ducts: an upper aluminium duct for hot-water circulation (Thermo Scientific, HAAKE S7), a lower aluminium duct for cold-water circulation (PolyScience, 9112E42E), and a middle duct for the MP–MO separation. Twelve holes, each with a diameter of $2\,\mathrm{mm}$ and a depth of $33.5\,\mathrm{mm}$ extending to the mid-plane of the channel cross-section, were drilled into the top and bottom plates for thermocouple (Type K) installation. The thermocouple holes were spaced $96\,\mathrm{mm}$ apart. To ensure good thermal contact between the thermocouple tips and the aluminium holes, thermal paste was applied inside the holes. The thermocouples were connected to a data logger (LabJack, T7-Pro) and the temperature transmitted to a computer for recording. Supplementary Fig. 8 shows the temperatures of the upper and lower walls measured using 12 thermocouples.

## Laser-based visualisation and image processing

The laser setup (Fig. 3a) was used for particle image velocimetry (PIV) measurements and visualisation of transport of MPs and *Artemia* across the rectangular channel (Supplementary Fig. 4a). A green line laser (geo-FENNEL, FPL L-GREEN; wavelength $515\,\mathrm{nm}$, power $< 1\,\mathrm{mW}$) was combined with a plano-convex cylindrical lens (TECHSPEC, Edmund Optics, fused silica, $50\,\mathrm{mm}$

effective focal length, $12.7\,\mathrm{mm} \times 12.7\,\mathrm{mm}$) to generate a laser sheet of about $1.5\,\mathrm{mm}$ in thickness for flow-field visualisation.

For PIV measurements, raw images were acquired using a CMOS camera (Basler ace2) equipped with a magnifying lens (AVENIR). The raw PIV images (e.g. Supplementary Fig. 4a(IV)) were analysed using the PIVlab toolbox in MATLAB to obtain the streamwise velocity profiles (Supplementary Fig. 4b). In addition, for the results presented in Section 2.3, the recorded videos were analysed using our developed MATLAB codes to quantify the separation ratios of *Artemia* and MPs along the length of the separation duct in single-constituent saline solutions (Supplementary Video 2b). Since *Artemia* counting was conducted under a $30\,\mathrm{K}$ temperature difference, bubbles formed near the heated top wall. Within the laser sheet at the centre of the duct, both bubbles and *Artemia* appear as similarly sized green objects, making it the most challenging part of the image-processing code to distinguish bubbles from *Artemia*. The tracking and counting of LPs at streamwise distances of $x = 190\,\mathrm{mm}$ to $260\,\mathrm{mm}$ from the inlet and HPs over the streamwise region $x = 280\,\mathrm{mm}$ to $350\,\mathrm{mm}$ are shown in Supplementary Video 2c and d, respectively.

## Multi-stage process for separation of *Artemia* from light and heavy microplastics

The three- and two-stage separation processes (Fig. 6a) have two phases. Phase A is characterised by low and/or moderate flow rates that aim to extract MOs from the bottom outlet and MPs from the top outlet. Phase B is characterised by a high flow rate that flushes MPs from both outlets. In the three-stage process, Phase A comprises two stages: mixture loading and residual MO removal, whereas the two-stage process does not remove residual MOs with moderate flow rates. The last stage for both processes is MP flushing (Phase B). In the two-stage configuration, the first stage (Phase A) was operated at $Q_2 = 241\,\mathrm{mL\,min^{-1}}$ ($u_2 = 16.5\,\mathrm{mm\,s^{-1}}$) or $Q_2 = 337\,\mathrm{mL\,min^{-1}}$ ($u_2 = 23.1\,\mathrm{mm\,s^{-1}}$). In the three-stage configuration, the same flow rates were applied to the second stage; while the flow rate of the first stage was very subtle, $Q_1 = 38\,\mathrm{mL\,min^{-1}}$ ($u_1 = 2.6\,\mathrm{mm\,s^{-1}}$), which is comparable with the swimming velocity of *Artemia*[37]. During the separation process, the temperature of the upper and lower walls were approximately fixed at 50 and $20\,^{\circ}\mathrm{C}$, respectively (Supplementary Fig. 8). In both configurations, the final stage was operated at a flow rate of $Q_3 = 1208\,\mathrm{mL\,min^{-1}}$, corresponding to a mean velocity of $u_3 = 82.9\,\mathrm{mm\,s^{-1}}$.

The mixtures collected from the top and bottom outlets during Phases A and B (four samples in total) were separately filtered through $100\,\mu\mathrm{m}$ meshes (Corning cell strainers) and dried for three days at room temperature to determine the combined mass of brine shrimp and microplastics. The samples were then treated with $5\,\mathrm{wt}\%$ to $6\,\mathrm{wt}\%$ sodium hypochlorite for $5\,\mathrm{h}$ to dissolve the *Artemia* nauplii, followed by a further three days of drying. The remaining mass was then measured to determine the MP mass (Fig. 6b and Supplementary Fig. 9e). The separation ratio of *Artemia* at the end of Phase A is calculated as

$$SR_{\mathrm{O,A}} = \frac{m_{\mathrm{O,btm,A}} - m_{\mathrm{O,top,A}}}{m_{\mathrm{O,btm,A}} + m_{\mathrm{O,top,A}}} \tag{2}$$

For MPs, the separation ratio of Phase A is given as

$$SR_{\mathrm{P,A}} = \frac{m_{\mathrm{P,top,A}} - m_{\mathrm{P,btm,A}}}{m_{\mathrm{P,btm,A}} + m_{\mathrm{P,top,A}}} \tag{3}$$

*Artemia* removal efficiency is written as

$$\eta_{\mathrm{O}} = \frac{m_{\mathrm{O,btm,A}}}{m_{\mathrm{O,btm,A}} + m_{\mathrm{O,top,A}} + m_{\mathrm{O,btm,B}} + m_{\mathrm{O,top,B}} + m_{\mathrm{O,R}}} \tag{4}$$

Finally, MP removal efficiency is given as

$$\eta_{\mathrm{P}} = \frac{m_{\mathrm{P,top,A}} + m_{\mathrm{P,btm,B}} + m_{\mathrm{P,top,B}}}{m_{\mathrm{P,btm,A}} + m_{\mathrm{P,top,A}} + m_{\mathrm{P,btm,B}} + m_{\mathrm{P,top,B}} + m_{\mathrm{P,R}}} \tag{5}$$

## Computational fluid dynamics

The transport of light and heavy MPs (abbreviated LP and HP, respectively) through the separation duct was simulated using the discrete phase model (DPM) in Ansys Fluent (2021 R2). The continuous saline phase was solved using the Eulerian approach, while the MPs were treated as discrete spherical particles and tracked in a Lagrangian framework[53]. Although the flow in the rectangular duct remains laminar over the entire range of flow rates considered (the corresponding Reynolds numbers are listed in Supplementary Table 3), the shear stress transport (SST) $k$–$\omega$ turbulence model[54] was employed to capture the inlet-induced vortical structures in the continuous phase.

The thermophysical properties of saline water were adopted from Ref. [55], expressed as functions of temperature, and implemented in Ansys Fluent through a user-defined function (UDF). The particle trajectories were determined by integrating the particle equation of motion, accounting for the drag force, gravitational force, and buoyancy. The particle density and diameter were specified using the nominal average values reported by the supplier. Momentum one-way coupling between the discrete and continuous phases was enabled, allowing the momentum exchange between the MPs and the surrounding saline flow to be considered. The convergence criteria were set to $10^{-3}$ for the continuity, $x$-, $y$-, and $z$-momentum, $k$, and $\omega$ residuals, and to $10^{-6}$ for the energy residual.

MPs were introduced at the duct inlet using a surface injection across the circular cross-section of the $4\,\mathrm{mm}$-diameter inlet pipe (Supplementary Fig. 10e), with the same flow rate and concentration as those used in the corresponding experimental conditions. The honeycomb diffuser and flow splitter (Supplementary Fig. 10e) were included in the simulations. For the results presented in Fig. 4 and Fig. 5d, f–h, the MP concentration was calculated from the total MP mass, including the masses collected from the top and bottom outlets and the residual MP mass in the separation duct, primarily deposited on the duct walls, divided by the corresponding total collected and residual solution volume. The reported MP concentration represents the average of all values obtained from the experiments. In all experiments, the initial MP concentration in the prepared suspension was $160\,\mathrm{mg\,L^{-1}}$. In addition, the particle size and density were prescribed according to the nominal mean properties of LP and HP.

CFD was used to visualise particle transport in a manner consistent with the experimental observations. Accordingly, each DPM parcel was defined to represent a spherical $390\,\mu\mathrm{m}$ MP, with the same particle density as in the experiment. The particle trajectories were tracked until they reached one of the two outlets. The numbers of particles exiting through the top and bottom outlets were recorded and used to determine the predicted separation ratio of each MP type. DPM simulations were performed under the same thermal and flow conditions as the corresponding experiments to evaluate the transport and separation behaviour of LP and HP along the rectangular duct. Lagrangian CFD methods for predicting particle trajectories can be highly sensitive to near-wall mesh resolution[56]. Accordingly,

mesh-independence (Supplementary Fig. 11a) and time-step independence (Supplementary Fig. 11b) studies were conducted. A mesh size of $1\,\mathrm{mm}$, an inflation-layer height of $390\,\mu\mathrm{m}$, and a time step of $0.2\,\mathrm{s}$ were selected for the simulations.

### Specific energy consumption analysis

The specific energy consumption (SEC) for the three- and two- stage processes is calculated based on the thermal energy required for operation. The thermal energy consumption (W) is the heat transfer rate $q$ from the upper to the cooled lower walls, which are fixed at $50.0\,^{\circ}\mathrm{C}$ and $20.0\,^{\circ}\mathrm{C}$, respectively.The operational performance is characterised by the remediation flow rate, ($Q_{\mathrm{L}}$), defined as the volume of microorganism–microplastic mixture processed during Stage 1 per unit of total separation-process time. The SEC is then

$$\mathrm{SEC} = \frac{\sum_{\mathrm{i}} q_{\mathrm{i}}}{Q_{\mathrm{L}}}, \tag{6}$$

where $q_{\mathrm{i}}$ denotes the heat transfer rate from the upper wall to the lower wall in Stage $i$. In the CFD modelling, the density, dynamic viscosity, and specific heat capacity of saline are considered as functions of temperature (Supplementary Fig. 2). Secondly, the required energy for stage $i$ for cooling the lower wall and heating the upper wall, based on the flow rate and fed volume $V$, is calculated as:

$$E_{\mathrm{i}} = \frac{(P_{\mathrm{cooling}} + P_{\mathrm{heating}})V_{\mathrm{i}}}{Q_{\mathrm{i}}}, \tag{7}$$

where $P$, $V$ and $Q$ denote power, volume and volumetric flow rate, respectively. Finally, the SEC of the multistage separation process is calculated as:

$$\mathrm{SEC} = \frac{E_{\mathrm{L_{O+P}}} + E_{(\mathrm{L_{O+P}F_O})} + E_{\mathrm{F_P}}}{V_{\mathrm{L_{O+P}}}}, \tag{8}$$

where $E_{(\mathrm{L_{O+P}F_O})}$ is zero for the two-stage process.

## Data availability

Source data is available via Figshare. All other data supporting the findings of this study are available from the corresponding author upon reasonable request.

## Acknowledgements

The authors thank Dr Mahdiar Taheri for his thoughtful discussions and constructive assistance with materials and *Artemia* imaging. The authors also thank Dr Shuqi Xu for her valuable feedback on the design of the separation duct, Dr Sahar Hosseini for her assistance with sessile drop test and microplastic SEM imaging, and Ms Alice Hutchinson for providing *Artemia* hatching procedure. This research was funded by the Department of Climate Change, Energy, the Environment and Water (DCCEEW) of Australia via the Marine Parks grant (Project ID: OMPG4-02) and was undertaken with the assistance of resources from the National Computational Infrastructure (NCI Australia), an NCRIS enabled capability supported by the Australian Government.

## Author contributions

M.V.B. designed and manufactured the experimental setups and components, developed the image-processing methods, developed an analytical model for MP transport, designed and performed the CFD simulations, characterised the microplastics and *Artemia*, designed

and conducted the experiments, proposed the multi-stage separation process and separation-efficiency metrics, analysed the data, and wrote the original draft. J.F.T. acquired funding, conceived the idea of using the thermal preference of *Artemia* for microplastic separation, designed the convectionless setup, designed the separation channel, designed the experiments, contributed to the definition of separation-efficiency parameters, analysed the results, supervised M.V.B., managed the project, and reviewed and edited the manuscript.

## Competing interests

The authors declare no competing interests.

## Additional information

**Supplementary information**. Additional material related to the description of the main findings has been included in the Supplementary Information document.

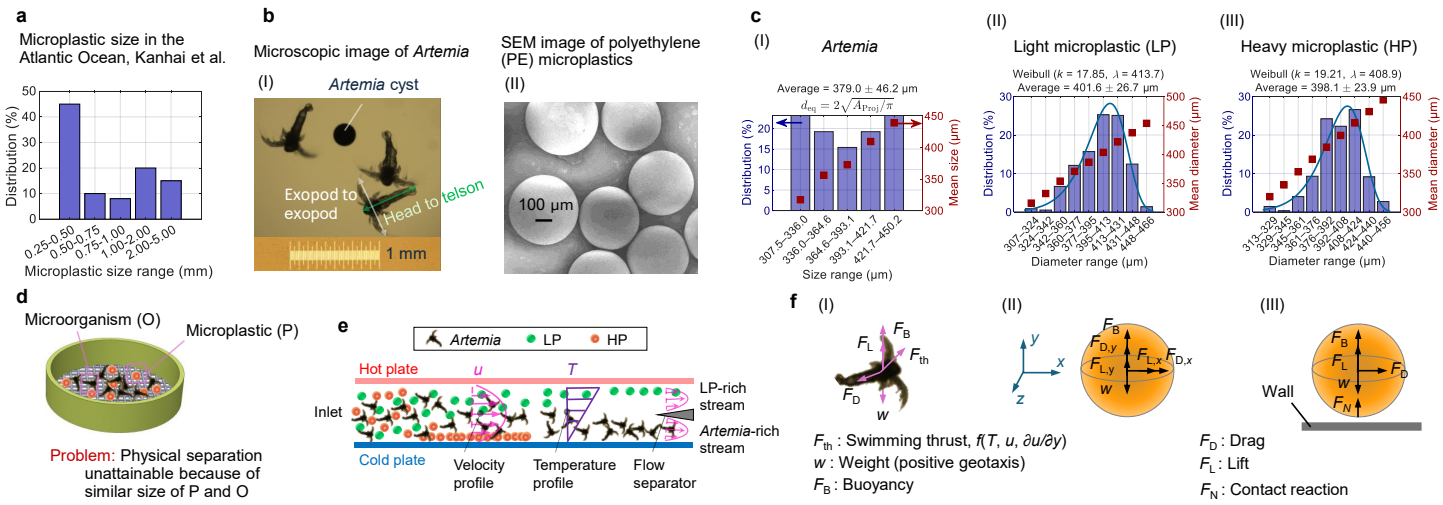



**Fig. 1 | Bio-friendly separation of microplastics from microorganisms: challenges, proposed solution and transport mechanisms.** **a**, Atlantic Ocean microplastic (MP) size distribution from Ref. [32]. **b**, Representative microscopic images of one-day old *Artemia* nauplii, also known as brine shrimp, with an unhatched *Artemia* cyst (I), and scanning electron microscopy (SEM) image of spherical polyethylene MPs with a diameter of approximately $390\,\mu\text{m}$ (II). **c**, Size distribution of *Artemia* nauplii and polyethylene MPs used in our experiments: equivalent diameter of one-day-old *Artemia* with an equivalent diameter of $379.0 \pm 46.2\,\mu\text{m}$ (I), diameters of light MPs, or LP, with a fitted Weibull size distribution ($k = 17.85$ and $\lambda = 413.7$) and average size of $401.6\,\mu\text{m} \pm 26.7\,\mu\text{m}$ (II), and heavy MPs, or HP, in addition to a fitted Weibull size distribution ($k = 19.21$ and $\lambda = 408.9$) and average size of $398.1 \pm 23.9\,\mu\text{m}$ (III). **d**, Key challenge in the bio-friendly physical separation of MP from living microorganisms (MOs). **e**, Schematic of the proposed bio-friendly separation strategy, combining thermotactic migration of *Artemia* under a temperature differential with hydrodynamic sorting of MPs governed by flow-rate-controlled residence time and near-wall transport. **f**, Free-body diagrams of a living MO (I), an MP moving far from the wall (II) and near the wall (III). The concentration of the plastic particles in saline is low enough ($< 0.02\,\text{wt}\%$) so that potential species interaction is neglected.

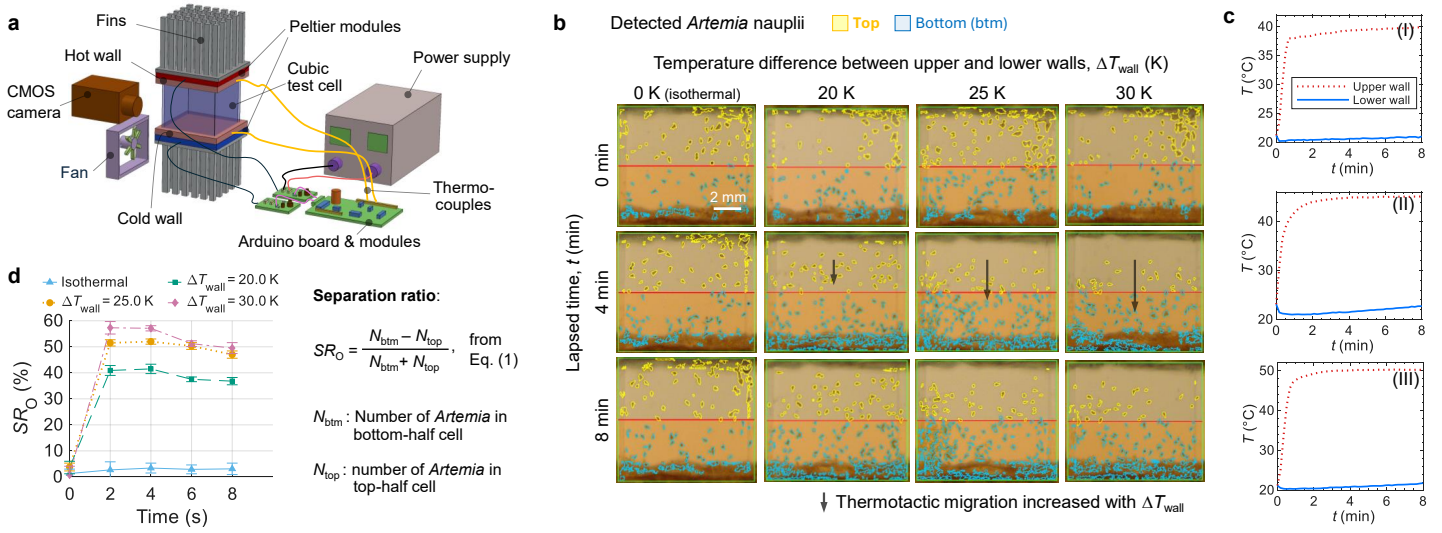



**Fig. 2 | Thermal response of *Artemia* (brine shrimp) in a convectionless environment.** **a**, Schematic of the convectionless setup used to generate a temperature differential in a $10\,\text{mm}$ cubic cell. **b**, Observed thermotactic migration of *Artemia* under an imposed temperature differential of $\Delta T_{\text{wall}}$ of 20, 25 and 30 K (lower plate temperature $T_{\text{low}} = 20.0\,^{\circ}\text{C}$). The isothermal case is included as a baseline. A count of *Artemia* nauplii in the top and bottom regions of the cell was performed by image processing; single run $n = 12$ – 15 images. **c**, Temperature evolution at the upper and lower walls for imposed temperature differences of $\Delta T_{\text{wall}} = 20\,\text{K}$ (I), 25 K (II) and 30 K (III). **d**, Separation ratio of *Artemia* in the cell, defined from the number of organisms in the top and bottom halves.

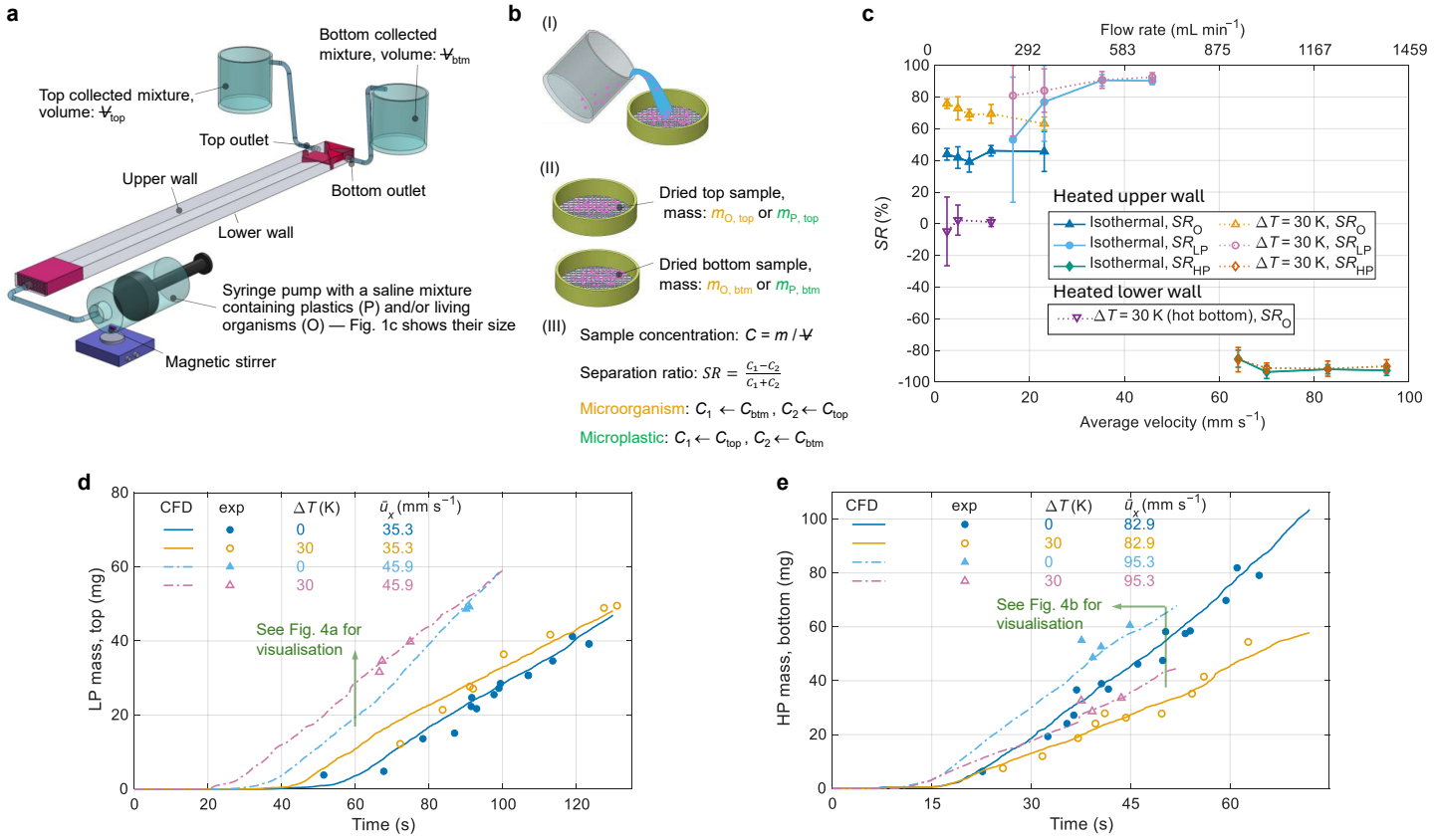



**Fig. 3 | Gravimetric separation analysis of individual species in saline: *Artemia*, light (LP) and heavy (HP) microplastics.** **a**, Schematic of the separation system comprising a syringe pump, a thermotactically controlled rectangular channel, and top/bottom outlet collection beaker. **b**, Sample-collection process: (I) separate sieving of the collected top and bottom stream samples, (II) drying of the sieved samples prior to mass measurement, and (III) separation ratio calculation based on concentration for living MOs and MPs. **c**, Separation ratio as a function of average fluid velocity and flow rate in the channel for the three saline mixtures: *Artemia*-only, light microplastic-only (LP) and heavy microplastic-only (HP). For the non-isothermal cases, the lower and upper wall temperatures are set to $20.0\,^{\circ}\mathrm{C}$ and $50.0\,^{\circ}\mathrm{C}$, respectively. The *Artemia* mixture is also tested in a thermally unstable case, heated from below, with a lower and upper temperatures of $50.0\,^{\circ}\mathrm{C}$ and $20.0\,^{\circ}\mathrm{C}$ to probe thermal migration under a gentle natural convection flow[52]. Supplementary Video 1 shows isothermal and non-isothermal *Artemia* transport in the channel up to $11.9\,\mathrm{mm\,s^{-1}}$. **d**, LP mass collected from the top outlet under isothermal and non-isothermal ($\Delta T_{\mathrm{wall}} = 30\,\mathrm{K}$) conditions for mean fluid velocities of $35.3\,\mathrm{mm\,s^{-1}}$and $45.9\,\mathrm{mm\,s^{-1}}$. **e**, HP mass collected from the bottom outlet, comparing isothermal and $\Delta T_{\mathrm{wall}} = 30\,\mathrm{K}$ cases for mean fluid velocities of 82.9 and $95.3\,\mathrm{mm\,s^{-1}}$.

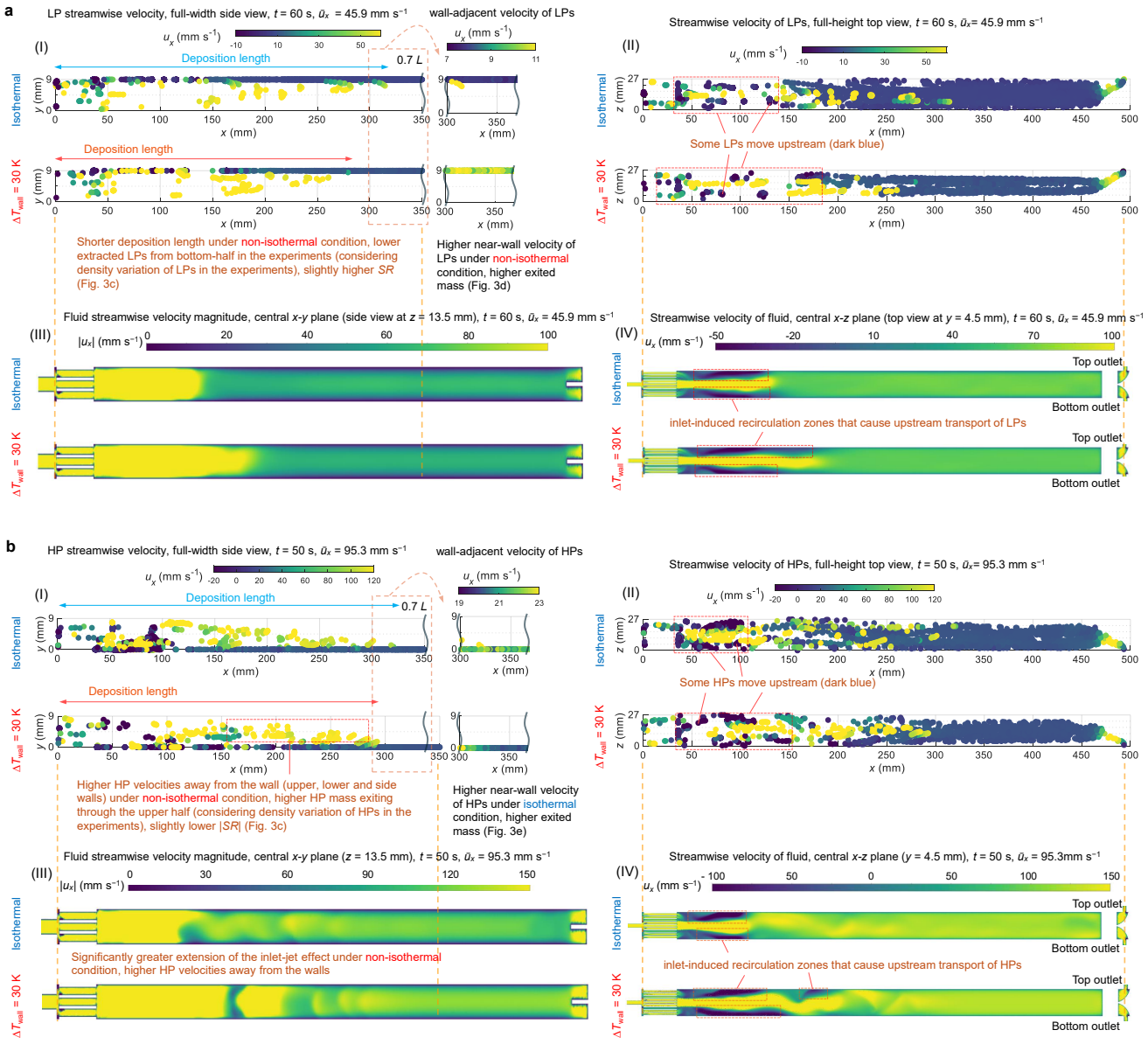



**Fig. 4 | Computational fluid dynamics (CFD) modelling of MP transport in the rectangular channel.** CFD results include the effect of temperature differential on inlet-jet-induced vortices, MP deposition length, and near-wall velocity. The temperature was maintained at 23.0 °C under isothermal case, while the lower and upper walls were maintained at 20 °C and 50 °C, respectively, under heated case. **a**, LP transport through the separation channel and the extension of inlet jet at $t = 60\,\mathrm{s}$ for a mean velocity of $\bar{u}_x = 45.9\,\mathrm{mm\,s^{-1}}$ under 23.0 °C isothermal and $\Delta T_{\mathrm{wall}} = 30\,\mathrm{K}$ heated conditions; (I) side view of the full-width ($z = 0$ to $z = 27\,\mathrm{mm}$) LP particle distribution coloured by particle the streamwise velocity, with near-wall particle velocities shown in the right insets, (II) top view of the channel showing the full-height ($y = 0$ to $y = 9\,\mathrm{mm}$) LP distribution and corresponding streamwise particle velocities, (III) absolute streamwise velocity contours of saline on the central $x$-$y$ plane ($z = 13.5\,\mathrm{mm}$), and (IV) streamwise velocity of saline through the central $x$-$z$ plane ($y = 4.5\,\mathrm{mm}$). **b**, Same analysis and thermal conditions as in the previous panel but for HP transport and a stronger flow at $\bar{u}_x = 95.3\,\mathrm{mm\,s^{-1}}$ and at $t = 50\,\mathrm{s}$.

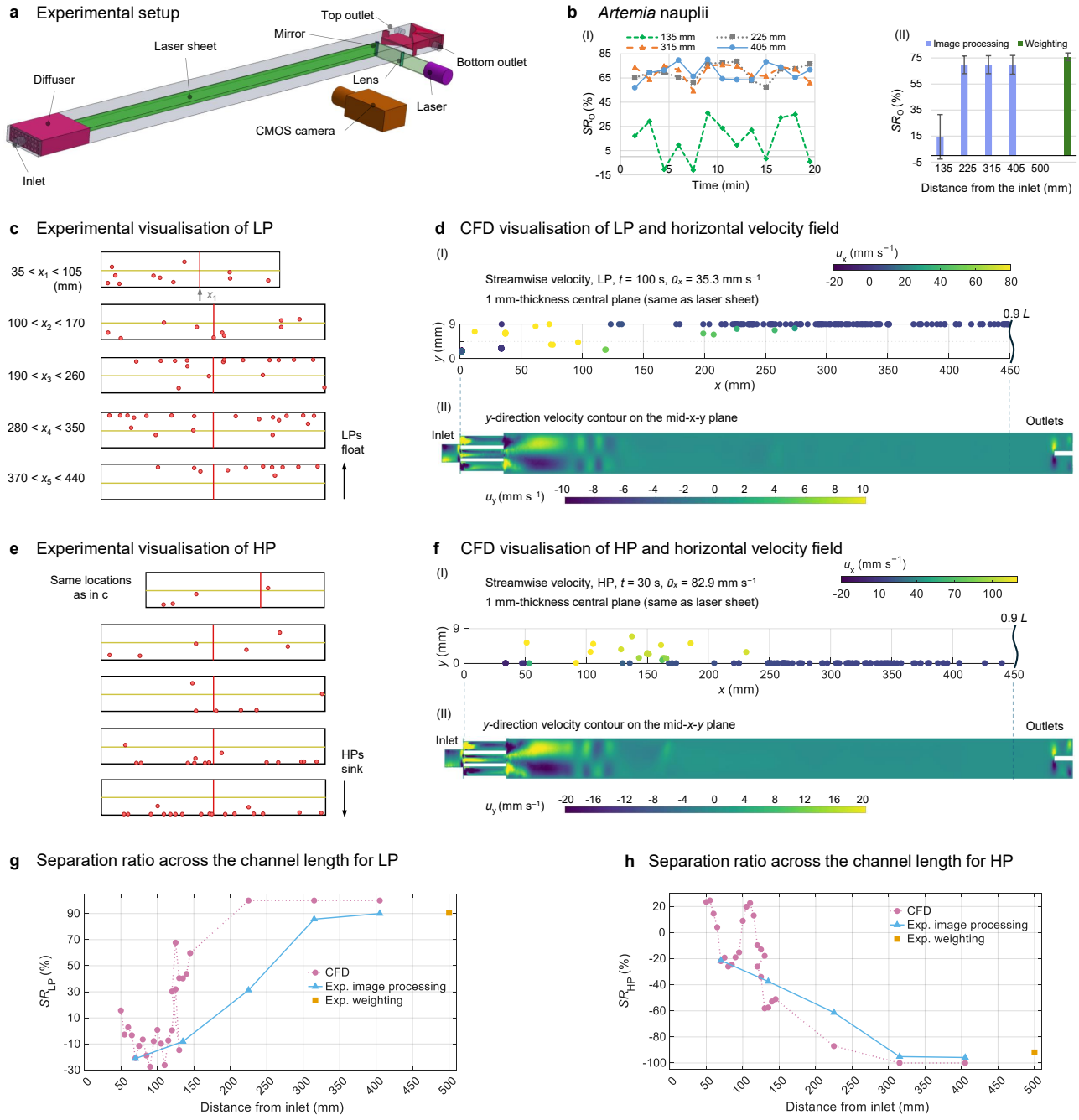



**Fig. 5 | Experimental and numerical visualisation of single constituents in saline.** **a**, Schematic of the visualisation using a laser sheet across the central streamwise plane of the rectangular channel flow. Supplementary Fig. 4a shows photos of the setup. **b**, Separation ratio of *Artemia* at $\Delta T_{\mathrm{wall}} = 30\,\mathrm{K}$, $T_{\mathrm{ave}} = 22.0\,^{\circ}\mathrm{C}$ and $\bar{u} = 2.6\,\mathrm{mm\,s^{-1}}$ at four streamwise positions ($x = 135$, 225, 315 and $405\,\mathrm{mm}$ from the inlet): (I) temporal *SR* and (II) time-averaged *SR*; $x = 500\,\mathrm{mm}$ denotes the outlet used for experimental sample collection. Raw and image-processed videos of *Artemia* transport at $x_5$ are provided in Supplementary Video 2b. **c**, Image-processed data of of LP distribution along the channel at five locations, $x_1 \rightarrow x_5$) at 70, 135, 225, 315 and $405\,\mathrm{mm}$ from the inlet. Dynamic LP transport at $x_3$ is provided in Supplementary Video 2c. **d**, CFD results for LP transport at $t = 100\,\mathrm{s}$ on the central $x$–$y$ plane. The particles inside the $1\,\mathrm{mm}$ thick laser sheet volume are plotted. **e**, Image-processing data of HP distribution along the channel. Dynamic HP transport at $x_4$ is shown in Supplementary Video 2d. **f**, CFD results for HP transport at $t = 30\,\mathrm{s}$. **g, h**, Time-averaged separation ratio of LP at $\bar{u} = 35.3\,\mathrm{mm\,s^{-1}}$ and HP at $\bar{u} = 82.9\,\mathrm{mm\,s^{-1}}$ under isothermal conditions, obtained by CFD and image processing; the data at $x = 500\,\mathrm{mm}$ were obtained by weighing the extracted mass in the gravimetric experiments.

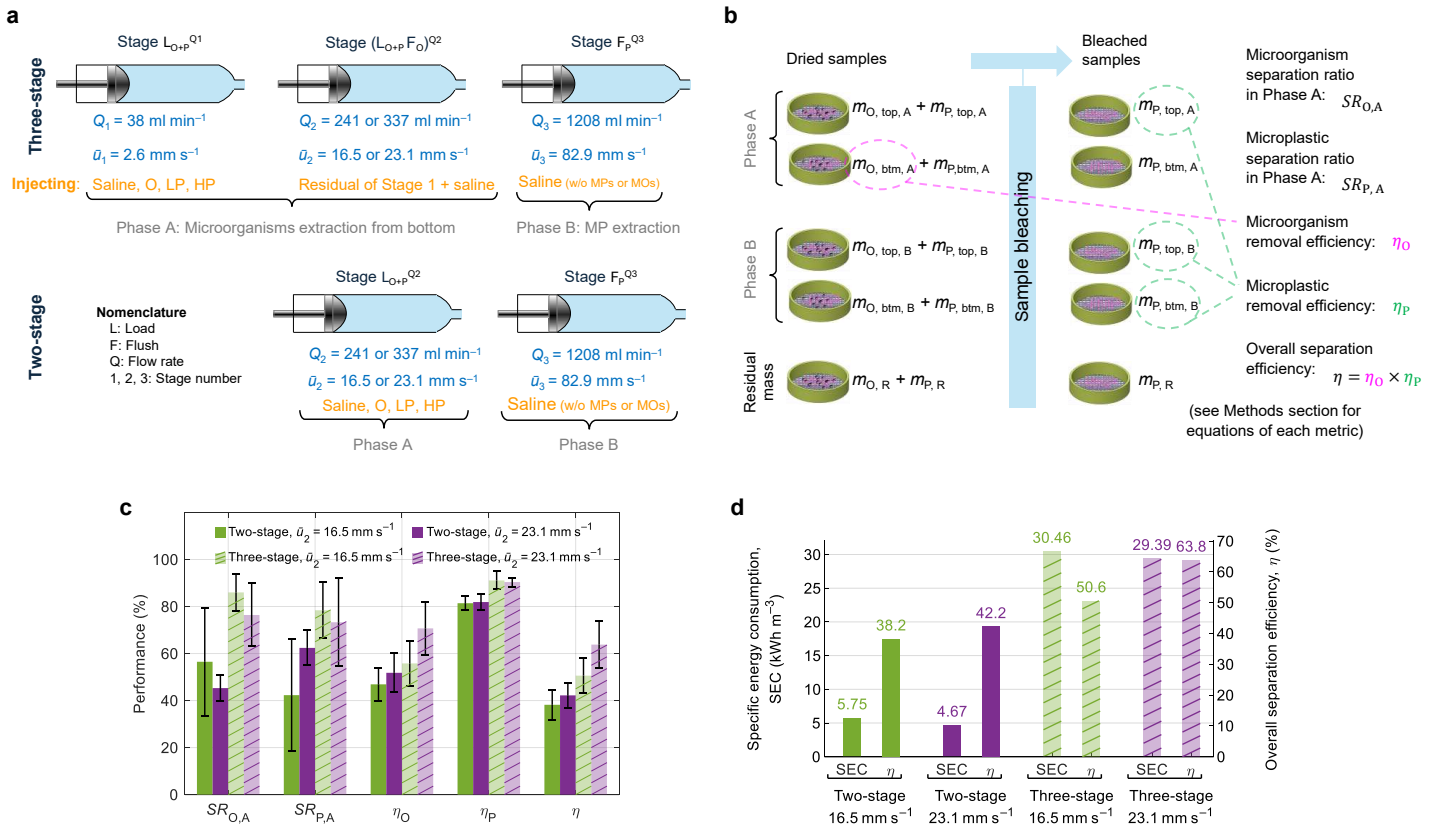



**Fig. 6 | Separation in a mixture of *Artemia*, light and heavy microplastics. a**, Pumping parameters for the three-stage and two-stage approaches. The volumetric flow rate $Q$ and average velocity $\bar{u}$ for each stage is indicated, together with the type of injected solution. **b**, Sample collection in Phase A, Phase B and the residual mass remaining in the channel after the process. After sieving, the samples were dried for three days and weighed to obtain the total mass of brine shrimp and microplastics; they were then bleached to dissolve the brine shrimp and dried for a further three days, after which the microplastic mass was determined. Performance in terms of different separation parameters: $SR_{O,A}$ and $SR_{P,A}$ are the separation ratios in Phase A of *Artemia* and MPs, respectively, $\eta_O$ and $\eta_P$ are the removal efficiencies of the *Artemia* and MPs, respectively, and the overall separation efficiency is $\eta = \eta_O \times \eta_P$. **c**, Mean values of the separation parameters for the three and two-stage processes. In the first stage of the two-stage process (mixture loading), the average velocity is either $\bar{u}_2 = 16.5\,\mathrm{mm\,s^{-1}}$ or $\bar{u}_2 = 23.1\,\mathrm{mm\,s^{-1}}$. In contrast, mixture loading is the three-stage process $\bar{u}_1 = 2.6\,\mathrm{mm\,s^{-1}}$ is followed by the second-stage (residual loading and microorganism flushing) at $\bar{u}_2 = 16.5\,\mathrm{mm\,s^{-1}}$ or $\bar{u}_2 = 23.1\,\mathrm{mm\,s^{-1}}$. **d**, Specific energy consumption and overall separation efficiency of the two- and three-stage processes.

# References


1. Choong, W. S., Hadibarata, T. & Tang, D. K. H. Abundance and distribution of microplastics in the water and riverbank sediment in Malaysia—A review. *Biointerface Research in Applied Chemistry* **11,** 11700–11712. DOI: 10.33263/BRIAC114.1170011712 (2021).

2. Shim, W. J. & Thomposon, R. C. Microplastics in the ocean. *Archives of environmental contamination and toxicology* **69,** 265–268. DOI: 10.1007/s00244-015-0216-x (2015).

3. Kvale, K. & Oschlies, A. Recovery from microplastic-induced marine deoxygenation may take centuries. *Nature Geoscience* **16,** 10–12. DOI: 10.1038/s41561-022-01096-w (2023).

4. Kvale, K., Prowe, A., Chien, C.-T., Landolfi, A. & Oschlies, A. Zooplankton grazing of microplastic can accelerate global loss of ocean oxygen. *Nature Communications* **12,** 2358. DOI: 10.1038/s41467-021-22554-w (2021).

5. Jambeck, J. R. *et al.* Plastic waste inputs from land into the ocean. *science* **347,** 768–771. DOI: 10.1126/science.12603 (2015).

6. Zhao, S. *et al.* The distribution of subsurface microplastics in the ocean. *Nature* **641,** 51–61. DOI: 10.1038/s41586-025-08818-1 (2025).

7. Xiao, W., Rene, E. R., Fang, W. & Zhang, P. Microplastics disrupt microalgal carbon fixation: Efficiency and underlying mechanisms. *Journal of Environmental Management* **404,** 129263. DOI: 10.1016/j.jenvman.2026.129263 (2026).

8. Wang, C., Jiang, L., Huang, W., Wang, C. & He, M. Light availability modulates the responses of the microalgae Desmodesmus sp. to micron-sized polyvinyl chloride microplastics. *Aquatic Toxicology* **249,** 106234. DOI: 10.1016/j.aquatox.2022.106234 (2022).

9. Serret, P. *et al.* Both respiration and photosynthesis determine the scaling of plankton metabolism in the oligotrophic ocean. *Nature Communications* **6,** 6961. DOI: 10.1038/ncomms7961 (2015).

10. Stubbins, A. Plastics in the marine carbon cycle: Pollution impacts. *Nature Sustainability* **8,** 1113–1114. DOI: 10.1038/s41893-025-01640-7 (2025).

11. Pang, Q. *et al.* The potential impacts of plastic on the marine carbon cycle. *Nature Sustainability* **8,** 1154–1163. DOI: 10.1038/s41893-025-01632-7 (2025).

12. Coppock, R. L. *et al.* Microplastics alter feeding selectivity and faecal density in the copepod, Calanus helgolandicus. *Science of the total environment* **687,** 780–789. DOI: 10.1016/j.scitotenv.2019.06.009 (2019).

13. Shore, E. A., DeMayo, J. A. & Pespeni, M. H. Microplastics reduce net population growth and fecal pellet sinking rates for the marine copepod, Acartia tonsa. *Environmental Pollution* **284,** 117379. DOI: 10.1016/j.envpol.2021.117379 (2021).

14. Cole, M. *et al.* Microplastics alter the properties and sinking rates of zooplankton faecal pellets. *Environmental science & technology* **50,** 3239–3246. DOI: 10.1021/acs.est.5b05905 (2016).

15. He, S. *et al.* Biofilm on microplastics in aqueous environment: Physicochemical properties and environmental implications. *Journal of Hazardous Materials* **424,** 127286. DOI: 10.1016/j.jhazmat.2021.127286 (2022).

16. Sui, Q. *et al.* Bioaccumulation of polycyclic aromatic hydrocarbons and their human health risks depend on the characteristics of microplastics in marine organisms of Sanggou Bay, China. *Journal of Hazardous Materials* **473,** 134622. DOI: 10.1016/j.jhazmat.2024.134622 (2024).

17. Pyl, M. *et al.* Evidence of microplastic-mediated transfer of PCB-153 to sea urchin tissues using radiotracers. *Marine Pollution Bulletin* **185,** 114322. DOI: 10.1016/j.marpolbul.2022.114322 (2022).

18. Pascall, M. A., Zabik, M. E., Zabik, M. J. & Hernandez, R. J. Uptake of polychlorinated biphenyls (PCBs) from an aqueous medium by polyethylene, polyvinyl chloride, and polystyrene films. *Journal of Agricultural and Food Chemistry* **53,** 164–169. DOI: 10.1021/jf048978t (2005).

19. González-Soto, N. *et al.* Effects of microplastics alone or with sorbed oil compounds from the water accommodated fraction of a North Sea crude oil on marine mussels (Mytilus galloprovincialis). *Science of the Total Environment* **851,** 157999. DOI: 10.1016/j.scitotenv.2022.157999 (2022).

20. Zhao, J. *et al.* Detection and characterization of microplastics and nanoplastics in biological samples. *Nature Reviews Bioengineering* **3,** 1019–1033. DOI: 10.1038/s44222-025-00335-0 (2025).

21. Giyahchi, M. & Moghimi, H. Sustainable solution for microplastic removal: Sequential biodegradation and detoxification of polyethylene terephthalate microplastics by two natural microbial consortia. *Ecotoxicology and Environmental Safety* **302,** 118738. DOI: 10.1016/j.ecoenv.2025.118738 (2025).

22. Akiyama, Y., Egawa, T., Koyano, K. & Moriwaki, H. Acoustic focusing of microplastics in microchannels: A promising continuous collection approach. *Sensors and Actuators B: Chemical* **304,** 127328. DOI: 10.1016/j.snb.2019.127328 (2020).

23. Sun, Z., Ma, C., Yu, C. & Li, Z. Microplastic separation and enrichment in microchannels under derivative electric field gradient by bipolar electrode reactions. *Scientific Reports* **14,** 4626. DOI: 10.1038/s41598-024-54921-0 (2024).

24. Ren, X., Breadmore, M. C. & Maya, F. Bidimensional dynamic magnetic levitation: sequential separation of microplastics by density and size. *Analytical Chemistry* **96,** 3259–3266. DOI: 10.1021/acs.analchem.3c02918 (2024).

25. Yuan, F. *et al.* A high-efficiency mini-hydrocyclone for microplastic separation from water via air flotation. *Journal of Water Process Engineering* **49,** 103084. DOI: 10.1016/j.jwpe.2022.103084 (2022).

26. Zhu, J. *et al.* Acceleration of photodegradation of microplastics in aquatic environments through laser pretreatment. *Optics Express* **33,** 45788–45806. DOI: 10.1364/OE.570298 (2025).

27. Wang, P. *et al.* Sustainable removal of nano/microplastics in water by solar energy. *Chemical Engineering Journal* **428,** 131196. DOI: 10.1016/j.cej.2021.131196 (2022).

28. Liu, M. *et al.* Environment-Friendly superhydrophobic sponge for highly efficient Oil/Water separation and microplastic removal. *Separation and Purification Technology* **319,** 124060. DOI: 10.1016/j.seppur.2023.124060 (2023).

29. Bhagwat, K. P., Rodrigue, D. & Romero-Zerón, L. Effective removal of microplastic particles from wastewater using hydrophobic bio-substrates. *Pollutants* **4,** 231–250. DOI: 10.3390/pollutants4020015 (2024).

30. Zheng, B., Wu, H., Zhang, M. & Lin, S. Removal of polystyrene microplastics from wastewater by Ti–Al electrode electrocoagulation under pulse current: Efficiency and mechanism. *Water Environment Research* **97,** e70057. DOI: 10.1002/wer.70057 (2025).

31. Shen, M. *et al.* Efficient removal of microplastics from wastewater by an electrocoagulation process. *Chemical Engineering Journal* **428,** 131161. DOI: 10.1016/j.cej.2021.131161 (2022).

32. La Daana, K. K., Officer, R., Lyashevska, O., Thompson, R. C. & O'Connor, I. Microplastic abundance, distribution and composition along a latitudinal gradient in the Atlantic Ocean. *Marine Pollution Bulletin* **115,** 307–314. DOI: 10.1016/j.marpolbul.2016.12.025 (2017).

33. Bermúdez, J. & Swarzenski, P. A microplastic size classification scheme aligned with universal plankton survey methods. *MethodsX* **8,** 101516. DOI: https://doi.org/10.1016/j.mex.2021.101516 (2021).

34. Southward, A. & Barrett, R. Observations on the vertical distribution of zooplankton, including post-larval teleosts, off Plymouth in the presence of a thermocline and a chlorophyll-dense layer. *Journal of Plankton Research* **5,** 599–618. DOI: 10.1093/plankt/5.4.599 (1983).

35. Henry, J. *et al.* A miniaturized electrothermal array for rapid analysis of temperature preference behaviors in ecology and ecotoxicology. *Environmental Pollution* **314,** 120202. DOI: 10.1016/j.envpol.2022.120202 (2022).

36. Singh, R. K. & Khandagale, P. Optimal water characteristics for commercial production of cysts of the brine shrimp, Artemia in salt ponds. *Crustaceana,* 913–923. DOI: 10.1163/156854006778815955 (2006).

37. Davenport, J. & Healy, A. Relationship between medium salinity, body density, buoyancy and swimming in Artemia franciscana larvae: constraints on water column use? *Hydrobiologia* **556,** 295–301. DOI: 10.1007/s10750-005-9118-7 (2006).

38. Sanjuan, A., Errarte, A. & Bou-Ali, M. M. Analysis of thermophoresis for separation of polystyrene microparticles in microfluidic devices. *International Journal of Heat and Mass Transfer* **189,** 122690. DOI: 10.1016/j.ijheatmasstransfer.2022.122690 (2022).

39. Grandjean, E. & Monkewitz, P. A. Experimental investigation into localized instabilities of mixed Rayleigh–Bénard–Poiseuille convection. *Journal of fluid mechanics* **640,** 401–419. DOI: 10.1017/S0022112009991467 (2009).

40. Tanguay, J. A., Reyes, R. C. & Clegg, J. S. Habitat diversity and adaptation to environmental stress in encysted embryos of the crustacean Artemia. *Journal of Biosciences* **29,** 489–501. DOI: 10.1007/BF02712121 (2004).

41. Clegg, J. S., Willsie, J. K. & Jackson, S. A. Adaptive significance of a small heat shock/$\alpha$-crystallin protein (p26) in encysted embryos of the brine shrimp, Artemia franciscana. *American Zoologist,* 836–847. DOI: 10.1093/icb/39.6.836 (1999).

42. McConnaughey, R. & Sulkin, S. Measuring the effects of thermoclines on the vertical migration of larvae of Callinectes sapidus (Brachyura: Portunidae) in the laboratory. *Marine Biology* **81,** 139–145. DOI: 10.1007/BF00393112 (1984).

43. Saito, S. *et al.* Characterization of TRPA channels in the starfish Patiria pectinifera: involvement of thermally activated TRPA1 in thermotaxis in marine planktonic larvae. *Scientific reports* **7,** 2173. DOI: 10.1038/s41598-017-02171-8 (2017).

44. Stride, B., Abolfathi, S., Bending, G. D. & Pearson, J. Quantifying microplastic dispersion due to density effects. *Journal of Hazardous Materials* **466,** 133440. DOI: 10.1016/j.jhazmat.2024.133440 (2024).

45. Yuan, Z., Nag, R. & Cummins, E. Ranking of potential hazards from microplastics polymers in the marine environment. *Journal of Hazardous Materials* **429,** 128399. DOI: doi.org/10.1016/j.jhazmat.2022.128399 (2022).

46. Rodríguez, A. M. *et al.* Vertical distribution and composition of microplastics and marine litter in the open ocean surrounding the Canary Islands (0–1200 m depth). *Marine Pollution Bulletin* **222,** 118836. DOI: 10.1016/j.marpolbul.2025.118836 (2026).

47. Wu, N., Grieve, S. W., Manning, A. J. & Spencer, K. L. Marine snow as vectors for microplastic transport: multiple aggregation cycles account for the settling of buoyant microplastics to deep-sea sediments. *Limnology and Oceanography* **70,** 899–910. DOI: 10.1002/lno.12814 (2025).

48. Jaffar, J., Shamsudin, R. N. R., Sulong, W. M. W., Hamid, K. H. & Faizul, E. A. S. E. Experimental Studies on Enhancing PV/T Collector Performance with Active Cooling Using Chilled Water. *International Journal of Heat & Technology* **43,** 1474. DOI: 10.18280/ijht.430424 (2025).

49. Busato, F., Lazzarin, R. & Noro, M. The control of renewable energies to improve the performance of multisource heat pump systems: A two-case study. *Applied Sciences* **11,** 6653. DOI: 10.3390/app11146653 (2021).

50. Abu-Hamdeh, N. H. & Alnefaie, K. A. Energy and exergy analysis and optimum working conditions of a renewable energy system using a transient systems simulation program. *Energy Exploration & Exploitation* **38,** 1248–1261. DOI: 10.1177/0144598720908071 (2020).

51. Coventry, J. & Lovegrove, K. Development of an approach to compare the 'value'of electrical and thermal output from a domestic PV/thermal system. *Solar Energy* **75,** 63–72. DOI: 10.1016/S0038-092X(03)00231-7 (2003).

52. Torres, J. F., Zhao, Y., Xu, S., Li, Z. & Komiya, A. Optical method for simultaneous high-resolution measurement of heat and fluid flow: The case of Rayleigh-Bénard convection. *Physical Review Applied* **14,** 054038. DOI: 10.1103/PhysRevApplied.14.054038 (2020).

53. Mahmoudi, O. & Shiri, Y. Effects of the radii of curvature and the connecting length on erosion behavior in sequentially connected elbows. *Scientific Reports* **15,** 20874. DOI: 10.1038/s41598-025-04961-x (2025).

54. Menter, F. R. Two-equation eddy-viscosity turbulence models for engineering applications. *AIAA journal* **32,** 1598–1605. DOI: 10.2514/3.12149 (1994).

55. Sharqawy, M. H., Lienhard, J. H. & Zubair, S. M. Thermophysical properties of seawater: a review of existing correlations and data. *Desalination and water treatment* **16,** 354–380. DOI: 10.5004/dwt.2010.1079 (2010).

56. Bass, K. & Longest, P. W. Recommendations for simulating microparticle deposition at conditions similar to the upper airways with two-equation turbulence models. *Journal of Aerosol Science* **119,** 31–50. DOI: 10.1016/j.jaerosci.2018.02.007 (2018).

## Supplementary Files

This is a list of supplementary files associated with this preprint. Click to download.

- SupplementaryInformation.pdf
- SupplementaryVideo1.mp4
- SupplementaryVideo2.mp4
- SupplementaryVideo3.mp4